Compaction localization and anisotropic permeability evolution

Computers and Geotechnics xxx (xxxx) xxx

Contents lists available at ScienceDirect

Computers and Geotechnics

journal homepage: www.elsevier.com/locate/compgeo

Research Paper

Compaction localization and anisotropic permeability evolution

Eleni Gerolymatou [a,*], Julia Leuthold [b]

[a] Chalmers University of Technology, Sweden
[b] Karlsruhe Institute of Technology, Germany

ARTICLE INFO

Keywords:
Compaction bands
Permeability evolution
Anisotropy
Pore collapse
Localization
Permeability anisotropy

ABSTRACT

The oedometric compaction of materials with collapsible structure is investigated from a numerical point of view. Such materials form planar zones of localized volumetric deformation that may or may not be accompanied by grain crushing. The purpose of the present work is to investigate the evolution of the permeability and its anisotropy as the result of the formation of compaction bands. The finite element method is used for the simulations with the commercial software ABAQUS. The mechanical response is calibrated on experimental results from the literature. Due to the localization of the deformation, the problem is not numerically stable and shows mesh dependence when a simple material model is used. To resolve the issue a nonlocal formulation is implemented. Drained oedometric tests are simulated. For the permeability different formulations are used, either ignoring the anisotropic evolution of the pore network or accounting for it. The results show that permeability anisotropy at the microscale needs to be considered, because otherwise the predicted reduction in permeability is qualitatively not in agreement with experimental results. On the whole, it is concluded that the permeability reduction following the formation of compaction bands can be highly anisotropic both at the micro and the macro scale.

1. Introduction

Compaction bands are planar zones characterized by high deformation in the direction parallel to the loading. They have been observed both *in situ* (Mollena and Antonellini, 1996; Sternlof, 2006) and in the laboratory (Bésuelle et al., 2000; Olsson, 1999; Baud et al., 2004). Localization of deformation in the form of compaction bands is known to take place in both porous rocks (Klein et al., 2001; Baxevanis et al., 2006; Leuthold et al., 2021) and several artificial materials (Gaitanaros et al., 2012; Barraclough et al., 2017) following compression. The mechanical response under triaxial loading exhibits as a rule a plateau after yield and hardening once the compaction process is complete (Vajdova et al., 2004; Baxevanis et al., 2006; Holcomb and Olsson, 2003), while the process of compaction band formation is sometimes accompanied by spontaneous unloadings (Vajdova et al., 2004; Leuthold et al., 2021). Observations under oedometric conditions also exist, but to a lesser extent(Castellanza et al., 2009, 2010). In the laboratory the phenomenon often initiates under triaxial conditions in the vicinity of the loading plates and propagates towards the midsection of the specimen (Louis et al., 2006; Castellanza et al., 2009; Leuthold et al., 2021), something that is most likely due to end plate friction or geometric constraints of the test. Experimental observations where this was not the case are also known in the literature (Kodaka et al., 2010). The conditions under which they appear were considered from a constitutive point of view by Issen and Rudnicki (2001).

The simulation of the formation of compaction bands, both alternating and continuous, is prone to mesh dependence, see for example (Chemenda, 2009; Dattola et al., 2015). Avoiding mesh dependence in the presence of strain softening requires the use of an internal length, for example in the form of a viscous (Das et al., 2013), a nonlocal (Bažant and Pijaudier-Cabot, 1988) or a micromorphic (Chambon et al., 2001) model.

It is reasonable to expect that the porosity reduction, with which the formation of compaction bands is generally associated, will be accompanied by a change in the hydraulic properties. Observations in the site show permeability reductions of several orders of magnitude (Ballas et al., 2012, 2013). A significant permeability reduction has been observed under triaxial conditions in the laboratory in several studies (Holcomb and Olsson, 2003; Vajdova et al., 2004; Baxevanis et al., 2006). Holcomb and Olsson (2003) found that the permeability reduction is more pronounced during the compaction process and less so before it initiates and after it is completed. In Vajdova et al. (2004) and

* Corresponding author.
E-mail address: eleni.gerolymatou@chalmers.se (E. Gerolymatou).

https://doi.org/10.1016/j.compgeo.2021.104173
Received 29 October 2020; Received in revised form 29 March 2021; Accepted 30 March 2021

Baxevanis et al. (2006) the tests were stopped before the end of the plateau. In all cases the permeability reduction was not in agreement with the scaling predicted by the law of Kozeny-Carman (Kozeny, 1927; Carman, 1937). There is little literature available on the permeability evolution in the direction normal to loading. Dautriat et al. (2011) performed constant K-tests in a triaxial setting and Leuthold (2020) performed oedometric compression tests. In both cases the permeability reduction was larger in the direction normal to loading in the presence of compaction than in the direction of the loading.

Few numerical simulations on the evolution of permeability as a result of localization of deformation are available (Bruno, 1994; Keehm et al., 2006; Nanda et al., 2020). None, to the authors' knowledge, are available considering the anisotropic evolution of permeability within the compaction bands. For the permeability parallel to the maximum principal load direction some equivalent continuum approaches are available (Holcomb and Olsson, 2003; Farquharson et al., 2017).

Much more literature is available on the simulation of permeability and permeability variation not considering localization. Among others, permeability prediction based on pore size distribution has been attempted using probability theory (Juang and Holtz, 1986) and capillary bundle models (Khaddour et al., 2018; Ecay et al., 2020) or analytical considerations (Pereira and Arson, 2013). Such approaches however cannot be directly incorporated into finite element simulations, as the permeabilities are calculated numerically. Under loading Shin et al. (2015) suggested a concept for anisotropic permeability evolution as a result of anisotropic strain. The pore network method was used and it was found that the permeability in the direction perpendicular to the major strain reduces faster, even though pore collapse was not considered and the pore size distribution remained the same. It was also found that under uniaxial deformation both the horizontal and vertical permeabilities decrease, albeit at different rates. In (Pietruszczak and Pande, 2012) a pipe network model was used to retrieve the relationship of permeability to the mean pore size and the pore size variation.

Empirical models link permeability to pressure and porosity, for example David et al. (1994). A wide variety of analytical models for the evaluation of the permeability as a function of quantities such as porosity and specific surface exist, most of which are generalizations of the Kozeny-Carman model (Kozeny, 1927; Carman, 1937). Examples include Childs and Collis-George (1950), Panda and Lake (1995), and Erol et al. (2017). Of these works in (Panda and Lake, 1995) an analytical expression for the permeability is given taking into account characteristics of the pore size distribution, such as variation and skewness. In all of these cases the possibility that the permeability may be anisotropic or may evolve anisotropically is not considered.

In the present work it is attempted to investigate whether the anisotropic permeability evolution observed in the laboratory in compacting rocks is a result of the non-uniformity of the hydraulic properties of the rock due to the formation of compaction bands or whether it is linked to permeability anisotropy within the compaction bands. To this end finite element simulations of oedometric compression of collapsible materials are performed and the global permeability is assessed under different assumptions for the permeability evolution of any given point. In Section 2 the methodology used is discussed, while Section 3 provides details on the assumptions made, the constitutive description and the calculations. The results are presented and discussed in Section 4. Conclusions are drawn last.

2. Methodology

As already mentioned, the aim of the present work is to assess to what extent the anisotropic evolution of permeability observed *in situ* and in the laboratory (Dautriat et al., 2011; Leuthold, 2020) is due to the geometry of the localization of deformation or due to the anisotropic evolution of the permeability at the microscale. In this section details of the method used are provided.

2.1. Investigation approach

A series of simulations of drained oedometric compression are performed, calibrated on a material that is prone to the formation of compaction bands. For the simulations the commercial software ABAQUS (Smith, 2009) is used with a User defined MATerial (UMAT), permeability controlled by USer Defined FieLDs (USDFLD) and an additional implementation to allow the use of nonlocal constitutive laws, which is described in the next subsection.

Four different types of tests were performed to assess the effect of the measurement of the permeability on the results. In type I the test is performed under drained conditions without permeability measurement. In types II and III the vertical and horizontal permeability are measured respectively, continuously during the test. Finally in type IV the mechanical loading is halted and the permeability is measured in the vertical and horizontal direction. During the measurement in test type IV the mechanical response is elastic. Each type of test is repeated under different assumptions for the local evolution of the permeability, namely isotropic or anisotropic.

Following the simulations, the mechanical and hydraulic response of the material for all tests is analyzed, compared and discussed. A comparison against experimental results from the literature is also performed in a qualitative manner.

2.2. Implementation of nonlocal regularization

For the simulation of the localization of deformation a nonlocal approach was selected. Regularization is necessary to ensure that the results do not depend on the numerical discretization. In the absence of regularization, the width of the compaction band would be equal to the size of one element. This non-physical behaviour can be resolved by using a non-simple continuum, in which case the width of compaction band is a material property and not one that depends on the numerical choice of mesh. To implement a nonlocal response it is necessary to access at each Gauss integration point information linked to the neighboring Gauss points, such as the internal variables. As a rule for simulations performed with the commercial code ABAQUS the material behavior is implemented in a user subroutine, called UMAT (User MATerial). This subroutine only has access to the information of the specific node that is being processed, so that the implementation of a non local model is not straighforward. The present section describes the procedure used when converting a UMAT to nonlocal for use in ABAQUS with a python script. The user defined subroutines UEXTERNALBD, URDFIL and UMAT are involved, as well as a user defined module, here called NLMODULE. The flowchart is given in Fig. 1.

The subroutine UEXTERNALDB is used here only once, at the beginning of the simulation and before the iteration begins. It allocates the table 'materials', in which the material to which each integration point belongs is later saved during the first call to the subroutine UMAT. It also allocates and populates the table 'l_c'. l_c(i) then yields the characteristic length of the material *i*.

The subroutine URDFIL is called at the end of each step. It populates the list of neighbours and the weights the first time that it is called in structure TAB_IP. For all subsequent steps it simply updates the value of the nonlocal state variables.

The subroutine get_nl returns the nonlocal version of the state variables, while the subroutine give_nl saves the updated list of state variables in the structure TAB_IP.

The above means that the non local version of internal variables, that is used in each step, corresponds to the previous time increment. This renders the regularisation explicit. Another option would be to update the nonlocal values during each increment and not solely at its end. In this way, some of the values of the state variables would belong to the current time increment and some to the previous one. It was selected not to use this approach, due to its lack of clarity. In addition, it would mean that the code cannot be run in parallel, which is however possible with

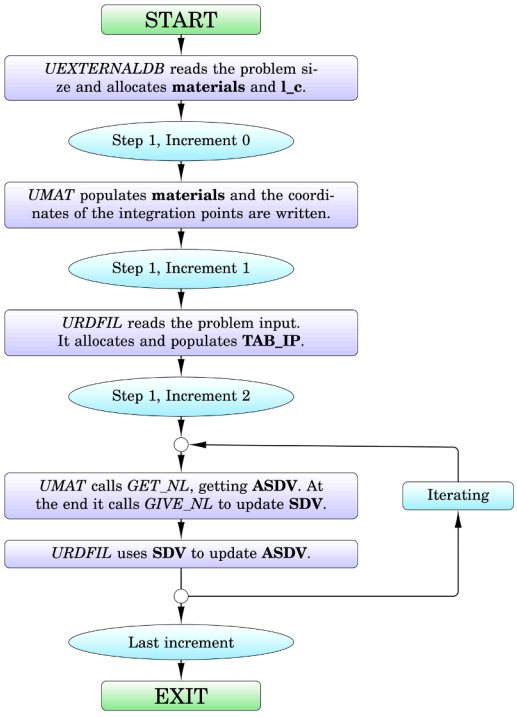

Fig. 1. Flowchart of the implementation of the nonlocal regularization in the numerical code ABAQUS.

the present formulation.

The averaged quantity is defined as

$$\widehat{u}(x) = \frac{\int_S h(x-s)u(s)ds}{\int_S h(x-s)ds} \tag{1}$$

Of course within the frame of a numerical scheme the distribution becomes discrete, so that, assuming $i = 1, \ldots, N$ to be the set of integration points within distance l_c of a given point, the above relationship becomes

$$\widehat{u}(x) = \frac{\sum_{i=1}^{N} h(x-x_i)\cdot u_i}{\sum_{i=1}^{N} h(x-x_i)} \tag{2}$$

It is worth remarking that a given integration point is also its own neighbor.

3. Theory and calculation

3.1. Mechanical response

The quantities used for the representation of the stress and the strain will be introduced with compression assumed positive. The material behavior is assumed to be isotropic, while the small strain hypothesis is made. The strain and the strain rate are decomposed additively into an elastic, reversible, and a viscoplastic, irreversible, part:

$$\underline{\epsilon} = \underline{\epsilon}^{e} + \underline{\epsilon}^{vp}, \quad \underline{\dot{\epsilon}} = \underline{\dot{\epsilon}}^{e} + \underline{\dot{\epsilon}}^{vp} \tag{3}$$

The viscoplastic strain rate is given by the flow rule

$$\underline{\dot{\epsilon}}^{vp} = \frac{1}{\eta}\left\langle \frac{f}{f_0} \right\rangle^{N} \frac{\partial f}{\partial \underline{\sigma}}, \tag{4}$$

following the commonly used Perzyna model (Perzyna, 1966), where $f_0 = p_c(t=0)$, N is assumed to be equal to unity, η is a viscosity parameter with units of time and

$$\langle u \rangle = \begin{cases} u, & \text{if } u > 0 \\ 0, & \text{otherwise.} \end{cases} \tag{5}$$

It is selected here to use a yield surface of the form

$$f = \frac{1}{f_0}\left[q^2 + M_f^2 h(p)(p-p_t)(p-p_c)\right]. \tag{6}$$

with $p = \frac{1}{3}\mathrm{tr}(\underline{\sigma}) = \frac{\sigma_{11}+\sigma_{22}+\sigma_{33}}{3}$ as the mean stress, $q = \sqrt{\frac{3}{2}}\left\|\underline{\sigma} - p\underline{\mathbf{I}}\right\| = \left\|\sqrt{\frac{3}{2}}\underline{\mathbf{s}}\right\|$ for the deviatoric stress and $\cos(3\theta) = \frac{3\sqrt{3}}{2}\frac{J_{3s}}{J_{2s}^{3/2}}$ is the definition of the Lode angle with $J_{2s} = \frac{1}{2}s_{ij}s_{ji}$ and $J_{3s} = \frac{1}{3}s_{ij}s_{jk}s_{ki}$. The multiplier M is defined as

$$M_f = M\gamma(\theta) \tag{7}$$

being thus a function of the Lode angle θ. The dependence on θ is introduced as

$$\gamma(\theta) = \frac{2c}{(1+c) - (1-c)\cos(3\theta)} \tag{8}$$

after Gudehus (1973), with

$$c = \frac{M_e}{M_c} \tag{9}$$

where M_c and M_e are the values of M in triaxial compression and extension, respectively.

For the dependence on the mean pressure the following expression is used:

$$h(p) = \exp\left[-\frac{1}{\beta}\left(\frac{p-p_t}{(p_c-p_t)} - a\right)^2\right] \tag{10}$$

In the above p_t is the tensile strength and p_c is the strength at isotropic compression and a and β are material parameters.

For the hardening law the approach by Castellanza and Nova (2004), which has been known to work well for bonded geomaterials, is used. It is assumed that

$$p_c = p_s + p_m \tag{11}$$

where p_s reflects the effect of fabric modification and p_m the effect of internal bonding. It is further assumed that

$$\dot{p}_s = \rho_s p_s\left(\dot{\epsilon}_v^p + \xi_s \dot{\epsilon}_q^p\right) \tag{12}$$

where ρ_s and ξ_s are material constants. In addition

$$\dot{p}_m = -\rho_m p_m\left(\left|\dot{\epsilon}_v^p\right| + \xi_m \dot{\epsilon}_q^p\right) \tag{13}$$

with $\epsilon_v = \epsilon_{11} + \epsilon_{22} + \epsilon_{33}$ for the volumetric strain and $\epsilon_q = \sqrt{\frac{2}{3}}\left\|\underline{\epsilon} - \frac{1}{3}\epsilon_v\underline{\mathbf{I}}\right\| = \sqrt{\frac{2}{3}}\left\|\underline{\mathbf{e}}\right\|$ for the deviatoric strain. The material parameters ρ_m and ξ_m control the rate of mechanical degradation of the cementation. In the current implementation p_s and p_m are nonlocal variables (Bažant and Pijaudier-Cabot, 1988). The tensile strength is considered to be analogous to the strength of the bonds, according to

$$p_t = -mp_m \tag{14}$$

where m is a dimensionless parameter.

The model was manually calibrated on an oedometric test on gas-beton after (Castellanza et al., 2009) and an incremental driver (Niemunis, 2017) was used for the calculation. The axial and radial stress, the stress ratio as a function of axial strain, the void ratio as a function of

axial stress and the stress path are given together with the fitting in Fig. 2. The parameters used for the fitting are given in Table 1.

As may be seen in Fig. 2, the resulting fit is rather good for the most part. Some small deviation is present, as far as the elastic branch is concerned. This deviation is plainer to see in Fig. 2c, where the void ratio is shown. This behavior is possibly due to the fact that the elastic branch, for strains smaller than 7%, is not truly linear, as shown in Fig. 2a. This could reflect a material property, but is most likely a result of imperfect initial contact of the specimen with the oedometric ring. The behavior could also be attributed to strain hardening. It is clear from the unloadings in Figs. 2a and 2b that the model fails to predict the change in the unloading response which results from compression. The parameter for the viscosity was not selected based on experimental results, as tests at different loading velocities were not available. Its value was selected equal to $\eta = 500$ s so that the results could not be distinguished from those resulting from the implicit integration of the non-viscous law at the loading velocities used here.

3.2. Permeability evolution

In what follows it is assumed that the solid fraction is not compressible. As a result the porosity can be expressed as a function of the initial porosity and the deformation. It should be noted that for compressible solid component this is not the case. For the sake of simplicity, the permeability is viewed as a function of its initial value and the deformation solely. As already discussed in the introduction, a large variety of formulations exist for the dependence of the permeability on porosity. Again for the sake of simplicity it is selected herein to adopt the formulation used in David et al. (1994), namely

Table 1
Parameters for the fitting of the experimental results.

E [MPa]	ν	α	β	M_f	m	ρ_s
60	0.15	1.3	2.0	2.0	0.2	10.75
ξ_s	ρ_m	ξ_m	p_s [MPa]	p_m [MPa]	N	η [s]
0.0	1.25	−1.0	0.15	3.75	1	500

$$k = k_0 \left(\frac{\phi}{\phi_0} \right)^n \tag{15}$$

where k is the current permeability, k_0 is the initial permeability, ϕ and ϕ_0 is the current and initial porosity respectively and n is a material parameter which in David et al. (1994) was found to range from 4.6 for Boise sandstone to 25 for Adamswiller sandstone. In the present work a value of 25 was selected. The initial value of the porosity for gasbeton is equal to 0.78. This formulation was used unaltered for the simulation performed under the assumption that the permeability evolution at the microscale is isotropic.

From the results of Pietruszczak and Pande (2012) and Shin et al. (2015) it is clear that the permeability at the microscale can evolve in an anisotropic manner and mainly depends on the deformation perpendicular to its direction. To capture this effect, simulations were also performed with an anisotropic evolution of the permeability at the microscale. To this end the concept of directional porosity is introduced, which is illustrated in Fig. 3. For each of the principal directions a cut of the body normal to the unit vector is to be imagined. For the calculation of the porosity in this direction the surfaces of the voids and the solids are used instead of the corresponding volumes. The permeability in the i,

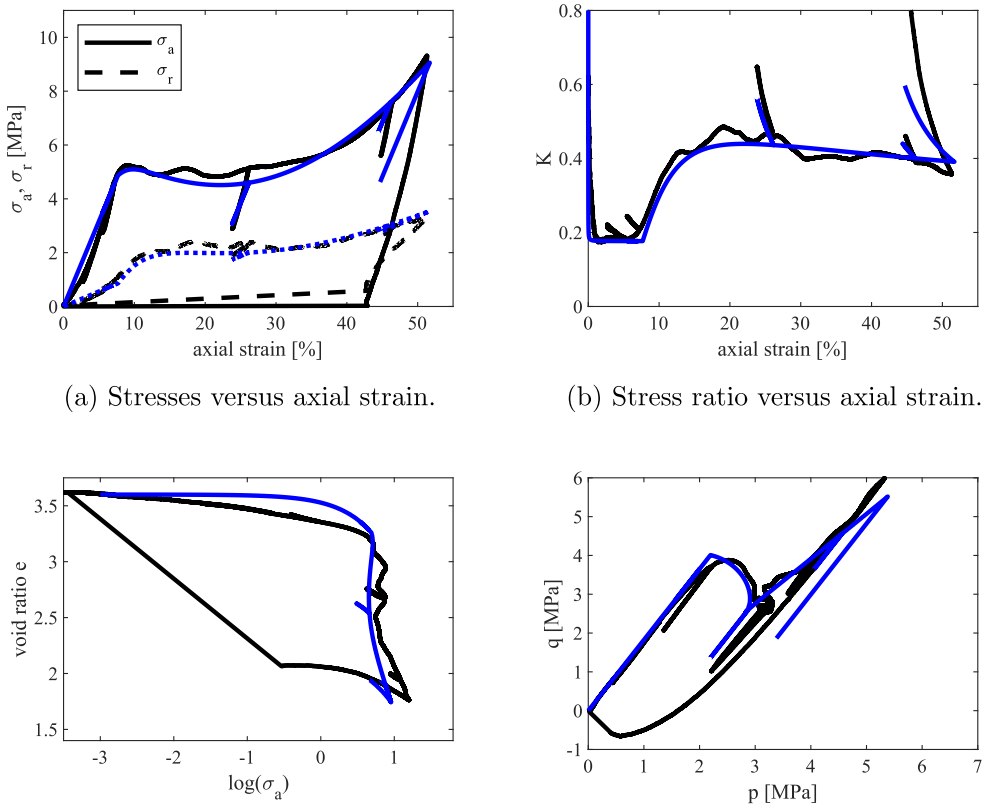

(a) Stresses versus axial strain.

(b) Stress ratio versus axial strain.

(c) Void ratio as a function of axial stress.

(d) Stress path.

Fig. 2. Experimental results from oedometer tests on Gasbeton (initial height 8.4 mm) after (Castellanza et al., 2009) (black) and numerical results from the calibration (blue).

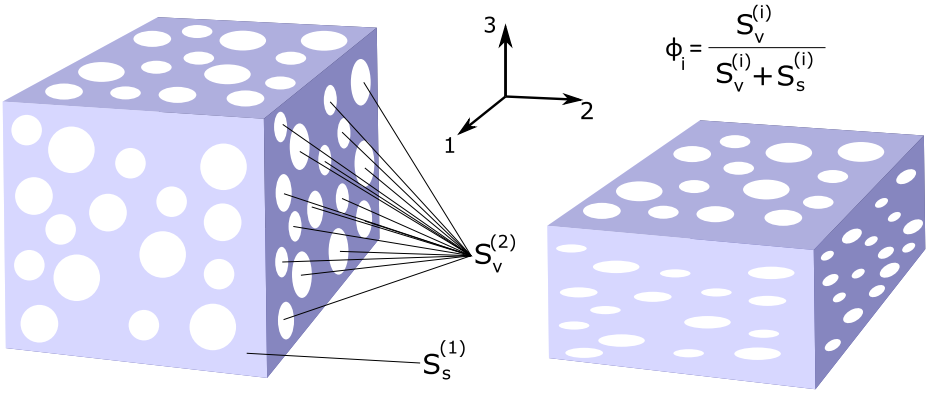

Fig. 3. Definition of directional porosity.

$i = 1, 2, 3$, direction was expressed assuming instead a directional porosity

$$\phi_i = \frac{S_v^{(i)}}{S_v^{(i)} + S_s^{(i)}} \tag{16}$$

where $S_v^{(i)}$ stands for the surface of voids perpendicular to the direction i and $S_s^{(i)}$ is the surface of solids perpendicular to the direction i. The second quantity is assumed to be constant, while for the first it is assumed that

$$S_v^{(i)} = S_{v,0}^{(i)}(1 - \epsilon_v + \epsilon_{ii}) - S_{s,0}^{(i)}(\epsilon_v - \epsilon_{ii}) \tag{17}$$

where Einstein summation was not used for the indices and compression is assumed positive.

The above formulation implies that under uniaxial strain the permeability remains constant in the direction of the deformation. This is also illustrated in Fig. 3, where for the deformed body on the right the surface of the voids in the vertical direction remains the same. This however is inaccurate, as shown in Shin et al. (2015). To incorporate this effect a further set of simulations, denoted as anisotropy with interaction, is performed based on the numerical results by Shin et al. (2015). Shin et al. (2015) measured the permeability of numerical samples under triaxial strain conditions for different ratios of the horizontal to the vertical strain using an enhanced pore network model. Their results for the normalized vertical and horizontal permeability are shown in Fig. 4 in black fitted with the relation

$$k_{ii} = k_0\left(1 - 4.6\mathrm{sgn}(\epsilon_v - \epsilon_{ii})\|\epsilon_v - \epsilon_{ii}\|^{0.85}\right)(1 - 4.0\epsilon_{ii}) \tag{18}$$

in blue where the first multiplier expresses the influence of the deformation in the plane normal to the direction of the permeability and the last multiplier expresses the influence of the deformation in the direction of the permeability. As can be seen in Fig. 4, the fit is excellent for compressive strains but tends to underestimate the variation of the permeability for extensile strains. As the planned simulations concern compression, this is not an issue in the present case. To account for the effect of the deformation in the direction of the permeability, the following relation for the permeability is used

$$k_{ii} = k_0\left(\frac{\phi_i}{\phi_0}\right)^n (1 - 4\epsilon_{ii}) \tag{19}$$

Though this is not necessarily realistic, since the material considered here is not that of Shin et al. (2015), it should provide an estimate at least from a qualitative point of view for the effect of the deformation in the direction of the permeability.

Above and in what follows, the tacit assumption has been made that deformation and permeability have the same principal directions. This is automatically satisfied if the initial permeability is isotropic.

3.3. Simulation setup

The simulations performed are of drained oedometric compression. The outline is shown in Fig. 5. In the out of plane direction the specimen has a depth of 1 element, while its height is equal to four times its width. All boundaries are assumed rigid and immovable with the exception of the upper boundary, at which the displacement is controlled.

The initial height of the specimen is equal to 5 mm, its width equal to 1.25 mm and the characteristic length is set equal to 0.5 mm. The initial stress state is isotropic with a mean pressure of 3 MPa. At the beginning of the test the specimen is completely saturated with no excess pore pressures. The maximum deformation amounts to 10% and is applied over 3600 s. The initial permeability is set to 10^{-14} m^2 and the physical

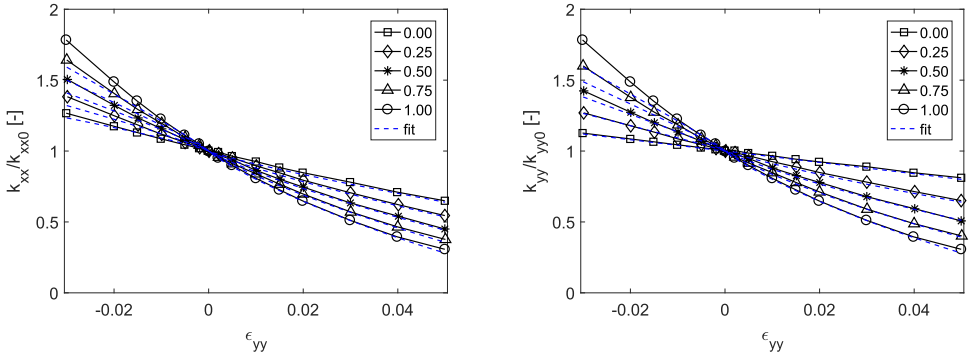

(a) Normalized horizontal permeability. (b) Normalized vertical permeability.

Fig. 4. Permeability evolution in the horizontal (a) and vertical (b) direction from numerical simulations modified after (Shin et al., 2015) (in black) and fit (in blue).

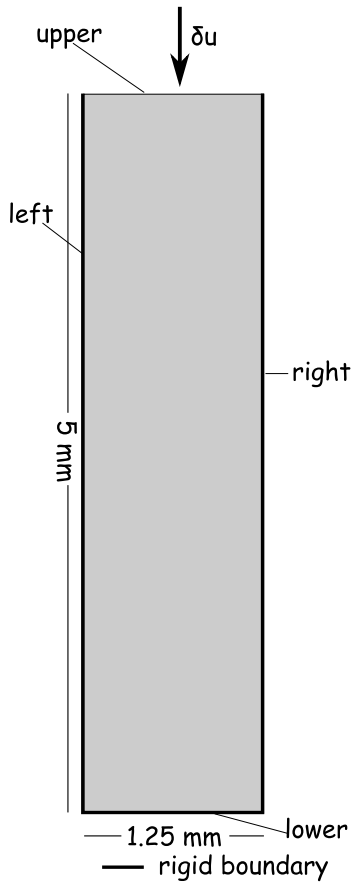

Fig. 5. Simulation setup.

properties of the fluid were those of water.

As far as the hydraulic boundary conditions are concerned, four types of tests were conducted:

- Type I: No permeability measurement, the left and right boundaries are impermeable and the pore pressure at the upper and lower boundary is set equal to 1 kPa.
- Type II: Permeability measurement in the vertical direction, the left and right boundaries are impermeable and the pore pressure at the upper and lower boundary is set equal to 11 kPa and 1 kPa respectively.
- Type III: Permeability measurement in the horizontal direction, the upper and lower boundaries are impermeable and the pore pressure at the left and right boundary is set equal to 11 kPa and 1 kPa respectively.
- Type IV: No permeability measurement during loading. The test is stopped at intervals of 1%. Then the permeability is measured in the vertical and horizontal direction sequentially using the pore pressures mentioned above. During the measurement the material is numerically set to an elastic response to ensure that no deformation takes place during the permeability measurement.

The global permeability is measured by making use of the flow rate and the pore pressure gradient. The aim is to ensure that the method of measurement does not influence the mechanical response or the results of the measurement.

4. Results and discussion

4.1. Code validation

In this section the results of the code are assessed to ensure that certain requirements are fulfilled. These are:

- the deformation should not localize in one element length
- the mechanical response should not be affected by the measurement of the permeability
- excess pore pressures should not build during the test
- the method of permeability measurement should not change the global permeability.

To ensure that the method of measurement does not affect the mechanical response, the mechanical behavior for all types of tests is compared. Fig. 6 (a) shows the axial stress plotted against axial strain for all four test types (I-IV), performed under the assumption that the evolution of the permeability is anisotropic without interaction calculated at the local point from Eqs. (16) and (17).

The curve progression and the value for the onset of the plastic deformation is similar for all test types. Small stress drops indicate the formation of discrete compaction bands in all test types and the onset of hardening is observed at 6% of axial strain for all calculations. This means the permeability measurement in the vertical and in horizontal direction has only at most a small influence on the mechanical behavior that can be neglected. The small differences between the stress curves can be attributed to different localization patterns, a result of the fact that randomly distributed defects were used to trigger localization.

Fig. 6b shows the comparison of the permeability measurements for types II to IV using Eqs. (16) and (17). It can be observed that the results are in excellent agreement, so it can be concluded that the method of the measurement of the permeability does not influence its value.

Fig. 7 shows the spatial distribution of the porosity in test type I at different values for the axial strain. It is clear that the deformation does not localize in one element length. As the mechanical behavior is similar for all test types the results are representative for all simulations. The localization begins in the middle of the sample, due to an artificial defect in the model. With increasing axial strain the compacted zone, characterized by smaller values for the void ratio, widens and propagates to the ends of the specimen. At an axial strain of 10% the whole specimen has experienced some compaction.

The boundary conditions are stationary, but since the local permeability is changing the analysis is transient. As a result, it is important to confirm that no pore overpressures are present. The maximum pore overpressure inside the sample was found to be negligible compared to the minimum principal stress, indicating that the formation of compaction bands does not lead to locally increased pore pressures that are high enough to influence the mechanical or the hydraulic response at least for the parameters used here.

All of the above indicates that the global permeability, determined by using the flow velocities at the boundaries in the vertical or in horizontal direction, is not influenced by the method of measurement. This implies that it is possible to use only test types II and III for the following numerical calculations.

4.2. Isotropic local permeability

In these calculations the permeability evolution is isotropic at the material point level using Eq. (15). Fig. 8 shows the global permeability in the vertical and horizontal direction plotted against axial strain. As expected for an isotropic permeability evolution, the curve progressions in the vertical and horizontal directions are similar to each other until the beginning of the plastic deformation. With further axial deformation the permeability in the vertical direction decreases faster than in the horizontal direction. Compared to the numerical model, the calculation

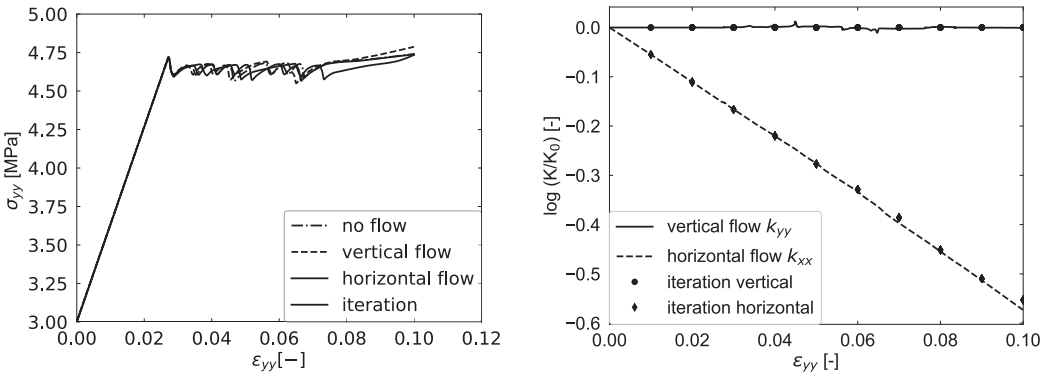

(a) Mechanical response of tests I-IV (b) Global permeability from numerical results of test types II-IV

Fig. 6. Comparison of the mechanical and the hydraulic behavior of the different test types.

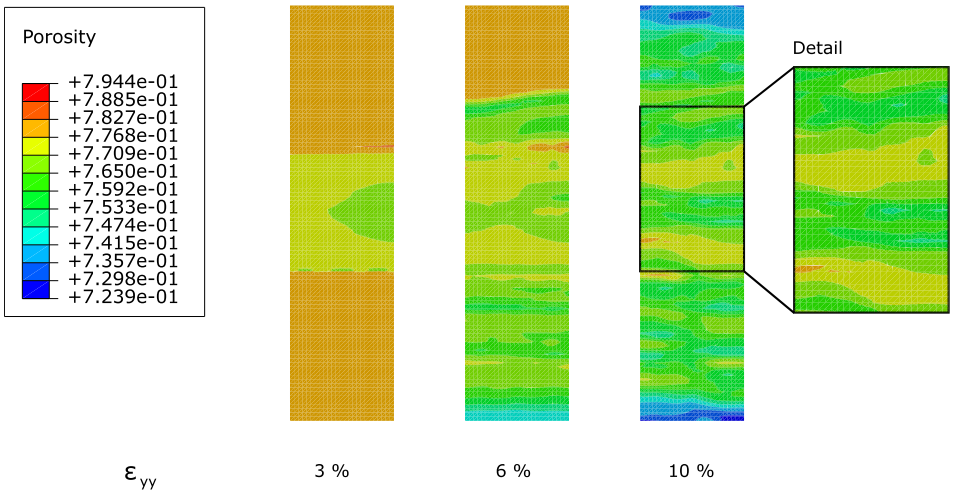

Fig. 7. Spatial distribution of porosity at different values for the axial strain.

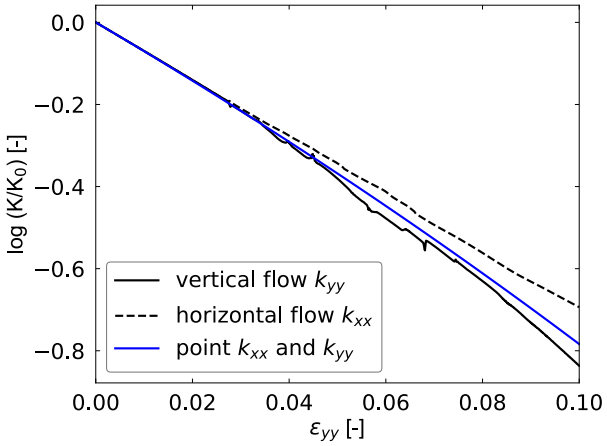

Fig. 8. Global permeability evolution in the vertical and horizontal direction (in black) and at the material point with isotropic permeability evolution at the material point (in blue).

for a material point, ignoring localization, overestimates the variation of the horizontal permeability and underestimates the variation in the vertical permeability. The reason for faster decrease of the permeability in the vertical direction is visible in the spatial distribution of the permeability at the end of each simulation that is shown in Fig. 9. Discrete compaction bands with smaller values for the local permeability are visible in the permeability distribution in vertical as well as in horizontal direction. The compaction bands form horizontal barriers to the flow in the vertical direction. Due to the isotropic evolution the permeability distribution has the same values in both directions. The differences in the spatial distribution of the permeability are linked to the differences in the location and order of formation of compaction bands between the results of test type II and test type III. The higher value of the global permeability in the horizontal direction is not in agreement with experimental results (Dautriat et al., 2011; Leuthold, 2020), which indicate that, in the presence of the formation of compaction bands, the permeability reduces faster in the horizontal direction.

4.3. Anisotropic local permeability

In the following the results of numerical calculations with the anisotropic permeability model are shown. First the results of numerical simulations are presented where the permeability in each direction depends only on the deformation in the directions normal to that of the permeability, in accordance with Eqs. (16,17). Fig. 10 (a) shows the global permeability in the vertical and horizontal direction plotted

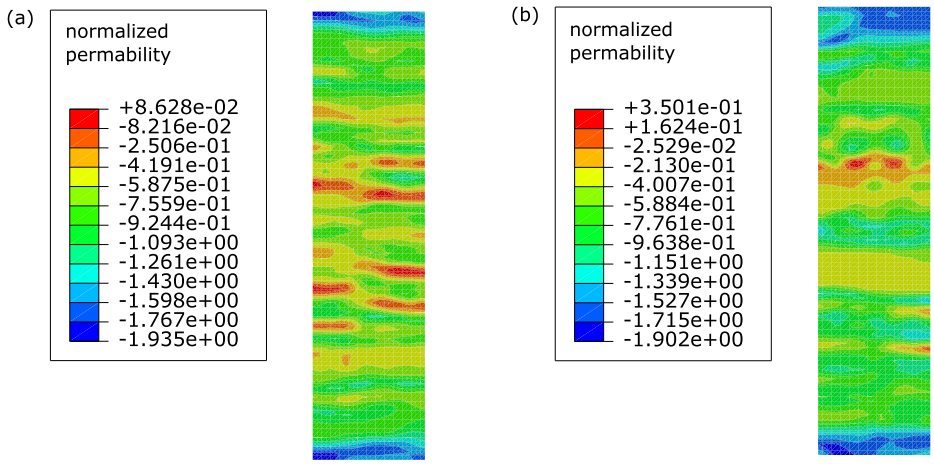

Fig. 9. Spatial distribution of normalized permeability in logarithmic scale from test type III (a) and from test type II (b) at an axial strain of 10%.

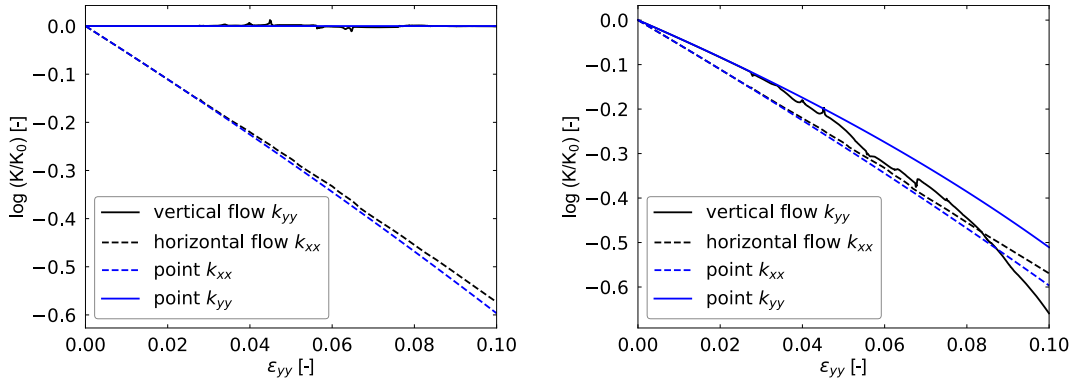

Fig. 10. Global permeability evolution in the vertical and horizontal direction with anisotropic permeability evolution with (a) and without (b) interaction.

against axial strain.

The evolution of the permeability in vertical and in horizontal direction is different. In the vertical direction the permeability stays practically constant, while in the horizontal direction it decreases significantly with increasing axial deformation. This means that the compaction process only influences the permeability in the horizontal direction. However in experimental results (Dautriat et al., 2011; Leuthold, 2020) the permeability in the direction of loading has been observed to also vary significantly with deformation, albeit to a lesser degree than the permeability normal to the loading. Compared to the numerical model, the calculation for a material point, ignoring localization, overestimates the variation of the horizontal permeability and captures well the lack of variation in the vertical permeability.

Fig. 11 shows the spatial distribution of the permeability in the

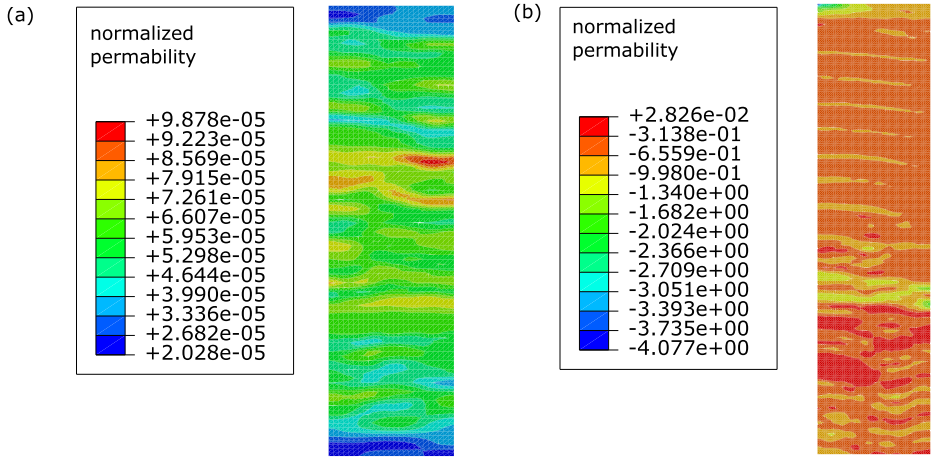

Fig. 11. Spatial distribution of normalized permeability in logarithmic scale in the horizontal direction (a) and in the vertical direction (b) at an axial strain of 10%.

vertical and the horizontal direction at an axial strain of 10%. The local permeability in the vertical direction is more homogeneous than in the horizontal direction. The effect of discrete compaction bands on the hydraulic properties is only visible in the distribution of the permeability in the horizontal direction and the values for the permeability in the horizontal direction are smaller than in the vertical direction.

To account for the effect of the axial deformation on the permeability in the vertical direction, Eq. (19) was used to describe the permeability evolution. Fig. 10b shows the evolution of the global permeability in the vertical and horizontal direction plotted against axial strain. The evolution of the permeability in the horizontal direction remains the same as in the previous simulation, but the permeability in the vertical direction differs. It decreases with increasing axial strain and the curve progression is different compared to the one in the horizontal direction. At an axial strain of 8% the permeability in vertical direction decreases more than in the horizontal direction. Compared to the numerical model, the calculation for a material point, ignoring localization, overestimates the variation of the horizontal permeability and underestimates the variation in the vertical permeability. Fig. 12 shows the spatial distribution of the permeability in the horizontal and vertical direction at an axial strain of 10%. The pattern of the local permeability is similar in both directions, because the hydraulic properties in both directions are affected by the axial deformation. Moreover, the values for the permeability are of the same order in both directions. These results are in good qualitative agreement with experimental results (Dautriat et al., 2011; Leuthold, 2020), contrary to the results of the previous two formulations, namely isotropic permeability evolution at the material point level and anisotropic evolution without taking into account the effect of the deformation in the direction of the flow.

Though no excess pore pressures are documented in the simulations, the effect of localization can be detected in the curve progression of the vertical permeability. Fig. 13 shows the permeability in the vertical direction and the axial stress plotted against axial strain. A comparison of the two curves shows that the small stress drops correlate with peaks in the vertical permeability evolution.

4.4. Scale effects

A factor that could affect the mechanical and the hydraulic behavior in the simulations is the scale effect. To investigate this effect simulations with a model that has twice the height but the same h/D ratio, the same element length and the same value for the internal length were performed, as well as simulations with a model of the initial size by an internal length reduced by half. Fig. 14 shows the permeability evolution in the vertical and horizontal direction for all three simulations plotted against axial strain. The permeability evolution in the horizontal

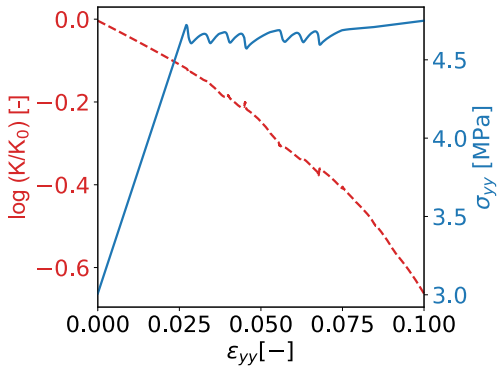

Fig. 13. Evolution of the global permeability in the vertical direction and axial stress as a function of axial strain.

direction is not affected by the size of the model, but the evolution of the permeability in the vertical direction is different for the different models, though the variations are small. In the simulations with the larger model the peaks in the curve progression of the permeability in the vertical direction are more pronounced, while for the smaller internal length they are less visible. This could be caused by random differences in the localization behavior in the simulation of test type II. It is however more likely that it is caused by the longer drainage path for the larger test. The results show that the difference in size or internal size does not influence the horizontal permeability, for which the drainage path is still significantly shorter than for test type II.

5. Conclusions

It is often assumed that the evolution of permeability with deformation can be evaluated using formulations that are isotropic at the point level. In the present work a series of simulations was performed to assess the suitability of this assumption. It was found that in the presence of compaction band formation it leads to qualitatively wrong results, with the permeability in the direction of loading varying to a greater degree than the permeability in the directions normal to the loading.

As a next step, only the deformation in the directions normal to the direction of the flow was assumed to have an influence on the permeability. Using this formulation it was found that the permeability in the direction of loading remained practically constant under oedometric conditions. This approach is also deemed unsuitable, as the variation of the permeability in the direction of loading is severely underestimated.

Finally, the deformation in the direction of flow was considered as well. This can be viewed as having an influence not so much on the

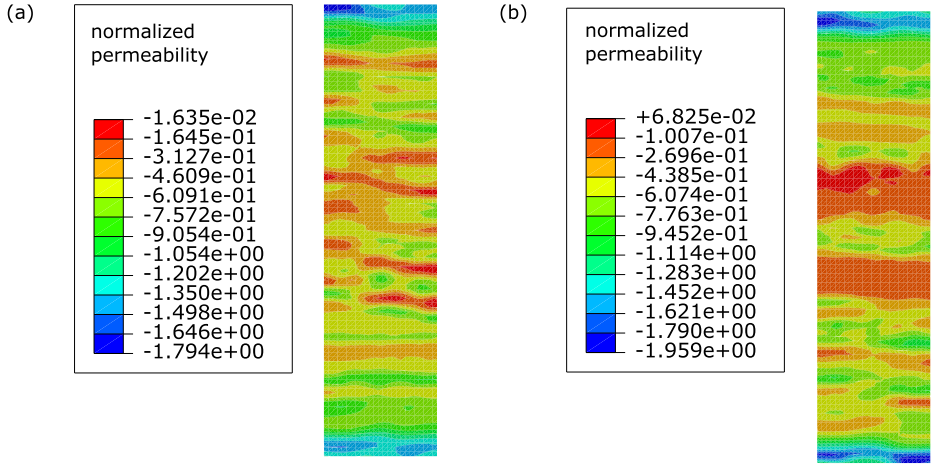

Fig. 12. Spatial distribution of normalized permeability in logarithmic scale in the horizontal direction (a) and in the vertical direction (b) at an axial strain of 10%.

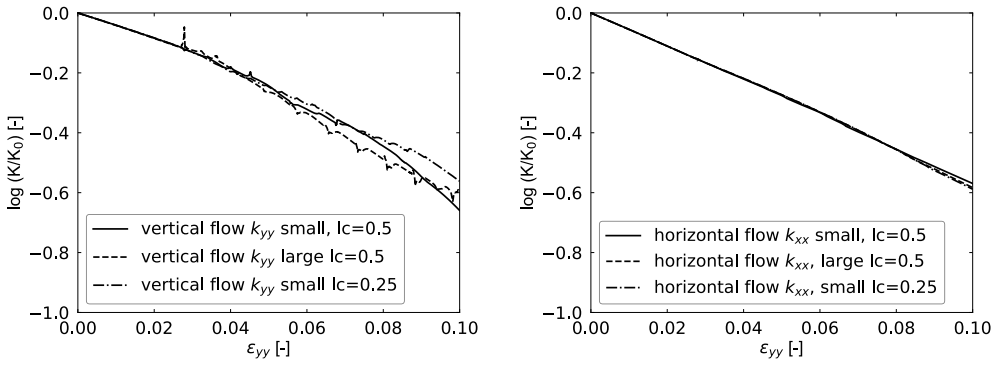

(a) vertical (b) horizontal

Fig. 14. Global permeability in the vertical (a) and horizontal (b) direction against axial strain from simulations with a height of 10 mm (large) and with a height of 5 mm (small) and the same h/d ratio and different values for the internal length l_c.

cross-section of pores in the direction of the flow, but on their connectivity and tortuosity, as discussed by Shin et al. (2015). In this case the results were in good qualitative agreement with experimental results from the literature (Dautriat et al., 2011; Leuthold, 2020).

The results show that, contrary to common practice, in order to correctly simulate the evolution of permeability in porous rocks under deformation, it is absolutely necessary to take into account the anisotropic evolution of the permeability induced through the deformation. The evolution of the permeability at the microscale, where the deformation can be considered uniform, should not only be anisotropic, but also account for the influence of the deformation in the direction of the flow. The point is of particular importance for example for deep reservoirs, where compaction takes place as a result of depletion and where permeability is important for further production or re-injection.

CRediT authorship contribution statement

Eleni Geolymatou: Conceptualization, Methodology, Validation, Formal analysis, Writing - original draft, Writing - review & editing. **Julia Leuthold:** Conceptualization, Methodology, Validation, Formal analysis, Investigation, Resources, Writing - review & editing, Visualization.

Declaration of Competing Interest

The authors declare that they have no known competing financial interests or personal relationships that could have appeared to influence the work reported in this paper.

References

Ballas, G., Soliva, R., Sizun, J.P., Benedicto, A., Cavailhes, T., Reynaud, S., 2012. The importance of the degree of cataclasis in shear bands for fluid flow in porous sandstone, Provence, France. AAPG Bull. 96, 2167–2186.

Ballas, G., Soliva, R., Sizun, J.P., Fossen, H., Benedicto, A., Skurtveit, E., 2013. Shear-enhanced compaction bands formed at shallow burial conditions; implications for fluid flow (Provence, France). J. Struct. Geol. 47, 3–15. https://doi.org/10.1016/j.jsg.2012.11.008.

Barraclough, T., Blackford, J., Liebenstein, S., Sandfeld, S., Stratford, T., Weinlander, G., Zaiser, 2017. Propagating compaction bands in confined compression of snow. Nature Phys. 13, 272–275.

Baud, P., Klein, E., Wong, T.F., 2004. Compaction localization in porous sandstones: spatial evolution of damage and acoustic emission activity. J. Struct. Geol. 26, 603–624. https://doi.org/10.1016/j.jsg.2003.09.002.

Baxevanis, T., Papamichos, E., Flornes, O., Larsen, I., 2006. Compaction bands and induced permeability reduction in Tuffeau de Maastricht calcarenite. Acta Geotech. 1, 123–135.

Bažant, Z., Pijaudier-Cabot, G., 1988. Nonlocal continuum damage, localization instability and convergence. J. Appl. Mech., Trans. ASME 55, 287–293.

Bésuelle, P., Desrues, J., Raynaud, S., 2000. Experimental characterisation of the localisation phenomenon inside a vosges sandstone in a triaxial cell. Int. J. Rock Mech. Min. Sci. 37, 1223–1237.

Bruno, M., 1994. Micromechanics of stress-induced permeability anisotropy and damage in sedimentary rock. Mech. Mater. 18, 31–48. https://doi.org/10.1016/0167-6636(94)90004-3.

Carman, P., 1937. Fluid flow through granular beds. Trans, Inst. Chem. Eng., London 15, 150–166.

Castellanza, R., Gerolymatou, E., Nova, R., 2009. Experimental observations and modelling of compaction bands in oedometric tests on high porosity rocks. Strain 45, 410–423.

Castellanza, R., Nova, R., 2004. Oedometric tests on artificially weathered carbonatic soft rocks. J. Geotech. Geoenviron. Eng. ASCE 130, 728–739.

Castellanza, R., Nova, R., Gerolymatou, E., Fusi, N., Barberini, V., Crosta, G., 2010. Evolution of compaction bands in high porosity soft rock. In: Rock Engineering in Difficult Ground Conditions - Soft Rocks and Karst - Proceedings of the Regional Symposium of the International Society for Rock Mechanics, EUROCK, pp. 249–254.

Chambon, R., Caillerie, D., Matsuchima, T., 2001. Plastic continuum with microstructure, local second gradient theories for geomaterials: localization studies. Int. J. Solids Struct. 38, 8503–8527.

Chemenda, A., 2009. The formation of tabulars compaction-band arrays: theoretical and numerical analysis. J. Mech. Phys. Solids 57, 851–868.

Childs, E., Collis-George, N., 1950. The permeability of porous materials. Proc. Roy. Soc. London A 201, 392–405.

Das, A., Nguyen, G., Einav, I., 2013. The propagation of compaction bands in porous rocks based on breakage mechanics. J. Geophys. Res.: Solid Earth 118, 1–18.

Dattola, G., di Prisco, C., Gerolymatou, E., 2015. Numerical and theoretical analysis of compaction banding in highly porous cemented materials. Int. J. Solids Struct. 75–76, 45–60.

Dautriat, J., Gland, N., Dimanov, A., Raphanel, J., 2011. Hydromechanical behavior of heterogeneous carbonate rock under proportional triaxial loadings. J. Geophys. Res.: Solid Earth 116, 1–26.

David, C., Wong, T.F., Zhu, W., Zhang, J., 1994. Laboratory measurement of compaction-induced permeability change in porous rocks: implications for the generation and maintenance of pore pressure excess in the crust. Pure Appl. Geophys. 143, 425–456.

Ecay, L., Grégoire, D., Pijaudier-Cabot, G., 2020. On the prediction of permeability and relative permeability from pore size distributions. Cem. Concr. Res. 133, 106074.

Erol, S., Fowler, S., Harcouët-Menou, V., Laenen, B., 2017. An Analytical Model of porosity–permeability for porous and fractured media. Transp. Porous Media 120, 327–358. https://doi.org/10.1007/s11242-017-0923-z.

Farquharson, J., Baud, P., Heap, M., 2017. Inelastic compaction and permeability evolution in volcanic rock. Solid Earth 8, 561–581.

Gaitanaros, S., Kyriakides, S., Kraynik, A., 2012. On the crushing response of random open-cell foams. Int. J. Solids Struct. 49, 2733–2743.

Gudehus, G., 1973. Elastoplastische Stoffgleichungen für trockenen Sand. Ingenieur-Archiv 42, 151–169.

Holcomb, D., Olsson, W., 2003. Compaction localization and fluid flow. J. Geophys. Res.: Solid Earth 108, 2290.

Issen, K., Rudnicki, J., 2001. Theory of compaction bands in porous rock. Phys. Chem. Earth (A) 26, 95–100.

Juang, C., Holtz, R., 1986. A probabilistic permeability model and the pore size density function. Int. J. Num. Anal. Methods Geomech. 10, 543–553.

Keehm, Y., Sternjof, K., Mukerji, T., 2006. Computational estimation of compaction band permeability in sandstone. Geosci. J. 10, 409–505.

Khaddour, F., Grégoire, D., Pijaudier-Cabot, G., 2018. A hierarchical model for the computation of permeation properties of porous materials and their enhancement due to microcracks. J. Eng. Mech. 144, 04017160.

Klein, E., Baud, P., Reuschlé, T., Wong, T., 2001. Mechanical behaviour and failure mode of Bentheim sandstone under triaxial compression. Phys. Chem. Earth (A) 26, 21–25.

Kodaka, T., Oka, F., Otani, J., Kitahara, H., Hirofumi, O., 2010. Experimental study of compaction bands in diatomaceous porous rock. In: Jacques, D., Gioacchino, V., Pierres, B. (Eds.), Advances in X-ray Tomography for Geomaterials. ISTE, London, pp. 1–6.

Kozeny, J., 1927. über kapillare leitung des wasser im boden. Sitzungsberichte Wiener Akademie 136, 271–306.

Leuthold, J., 2020. Hydromechanical Anisotropy in Porous Rock Material. Ph.D. thesis. Karlsruhe Institute of Technology.

Leuthold, J., Gerolymatou, E., Vergara, M., Triantafyllidis, T., 2021. Effect of compaction banding on the hydraulic properties of porous rock - Part I: Experimental investigation. Rock Mech. Rock Eng. 1–13.

Louis, L., Wong, T., Baud, P., Tembe, S., 2006. Imaging strain localization by X-ray computed tomography: discrete compaction bands in Diemelstadt sandstone. J. Struct. Geol. 28, 762–775. https://doi.org/10.1016/j.jsg.2006.02.006.

Mollena, P., Antonellini, M., 1996. Compaction bands: a structural analog for anti mode I cracks in aeolian sandstone. Tectonophysics 267, 209–228.

Nanda, K., Vaishakh, T., Das, A., Misra, S., 2020. Hydro-mechanical response in porous rocks during localized deformation: finite element analysis. J. Struct. Geol. 130, 103909.

Niemunis, A., 2017. Incremental Driver. https://soilmodels.com/idriver.

Olsson, W., 1999. Theoretical and experimental investigation of compaction bands in porous rock. J. Geophys. Res.: Solid Earth 104, 7219–7228. https://doi.org/10.1029/1998JB900120.

Panda, M., Lake, L., 1995. A physical model of cementation and its effects on single-phase permeability. Am. Assoc. Pet. Geol. Bull. 79, 431–443. https://doi.org/10.1016/0148-9062(96)83919-2.

Pereira, J., Arson, C., 2013. Retention and permeability properties of damaged porous rocks. Comput. Geotech. 48, 272–282.

Perzyna, P., 1966. Fundamental problems in viscoplasticity. Adv. Appl. Mech. 9, 243–377. https://doi.org/10.1016/S0065-2156(08)70009-7. cited By 848.

Pietruszczak, S., Pande, G., 2012. Description of hydraulic and strength properties of anisotropic geomaterials. Studia Geotechnica et Mechanica XXXIV, 3–16.

Shin, H., Kim, K., Pande, G., 2015. On computation of strain-dependent permeability of rocks and rock-like porous media. Int. J. Numer. Anal. Meth. Geomech. 39, 821–832. https://doi.org/10.1002/nag.2334.

Smith, M., 2009. ABAQUS/Standard User's Manual, Version 2017. Dassault Systèmes Simulia Corp, United States.

Sternlof, K., 2006. Structural Geology, Propagation Mechanics and Hydraulic Effects of Compaction Bands in Sandstone. Ph.D. thesis. Stanford University.

Vajdova, V., Baud, P., Wong, T., 2004. Permeability evolution during localized deformation in Bentheim sandstone. J. Geophys. Res.: Solid Earth 109, 1–15. https://doi.org/10.1029/2003JB002942.